

# Learning Correlated Astrophysical Foregrounds with Denoising Diffusion Probabilistic Models

Karthik Prabhu<sup>a,1</sup> Srinivasan Raghunathan<sup>b</sup> Ethan B. Anderes<sup>c</sup>  
Lloyd E. Knox<sup>a</sup>

<sup>a</sup>Department of Physics & Astronomy, University of California, One Shields Avenue, Davis, CA 95616, USA

<sup>b</sup>Center for AstroPhysical Surveys, National Center for Supercomputing Applications, Urbana, IL, 61801, USA

<sup>c</sup>Department of Statistics, University of California, One Shields Avenue, Davis, CA 95616, USA

E-mail: [kprabhu@ucdavis.edu](mailto:kprabhu@ucdavis.edu)

**Abstract.** Extragalactic foregrounds – most notably the Cosmic Infrared Background (CIB) and the thermal Sunyaev–Zel’dovich (tSZ) effect — exhibit complex, non-Gaussian structure and correlations that can bias analyses of small-scale cosmic microwave background (CMB) temperature anisotropies. These foregrounds can introduce mode coupling ( $\ell - \ell'$  mixing) at small-scales (multipoles  $\ell \geq 3000$ ) that mimic true lensing signals, thereby complicating analyses such as CMB lensing reconstruction. We present a novel approach to learn their full joint distribution using Denoising Diffusion Probabilistic Models (DDPMs) trained on paired CIB–tSZ patches at 150 GHz, from the Agora suite of extragalactic sky simulations. While simulations like Agora, which are based on N-body calculations, can take thousands of CPU hours, DDPM can synthesize realistic CIB–tSZ patches that faithfully reproduce both auto- and cross-spectral statistics of the 2-point, 3-point, and 4-point correlation functions, in a matter of seconds. We further demonstrate matching pixel-value histograms and Minkowski functionals, confirming that conventional non-Gaussian benchmarks are also satisfied. This framework provides a powerful generative tool for forward-modeling correlated extragalactic foregrounds in current and future CMB analyses. Although we mainly demonstrate the joint modeling of tSZ and CIB at a single frequency, we also include examples of its extension to multiple frequencies, showing that the framework can learn the spectral energy distributions (SEDs) across different bands. While establishing DDPMs as a promising tool for addressing foreground contamination in next-generation CMB surveys, we also outline remaining challenges to their practical deployment in analysis pipelines, such as scaling to larger sky areas and reliance on the underlying cosmological and astrophysical assumptions in the simulations used for training. Our code and plotting scripts can be found on this [GitHub repo](#)<sup>9</sup>.

---

## Contents

<b>1</b>	<b>Introduction</b>	<b>1</b>
<b>2</b>	<b>Data</b>	<b>3</b>
2.1	Agora simulations	3
<b>3</b>	<b>Methodology</b>	<b>4</b>
3.1	DDPM Framework	4
3.2	Summary Statistics	5
<b>4</b>	<b>Results</b>	<b>7</b>
4.1	Visual Inspection	7
4.2	Stacked tSZ profiles	7
4.3	Power Spectra comparison	9
4.4	Pixel Intensity Histograms	9
4.5	Minkowski Functionals	10
4.6	Bispectrum and Trispectrum	11
<b>5</b>	<b>Discussion</b>	<b>11</b>
5.1	Applications	12
5.2	Real-world challenges	13
5.3	Comparison with other generative modeling approaches	14
<b>6</b>	<b>Conclusions</b>	<b>14</b>
<b>A</b>	<b>Training Details</b>	<b>16</b>
<b>B</b>	<b>Correlations across frequency</b>	<b>16</b>
<b>C</b>	<b>Higher order auto- and cross- moments</b>	<b>17</b>

---

## 1 Introduction

Millimeter-wave observations of the cosmic microwave background (CMB) have been central to the success of modern cosmology, providing a precise view of the early universe and placing stringent constraints on the parameters of the  $\Lambda$ CDM model. In addition to the primordial fluctuations, the CMB also carries imprints of its interactions with large-scale structure through secondary anisotropies, which are emerging as powerful probes of both cosmology and astrophysics. Foremost among these secondary effects are gravitational lensing and the kinematic and thermal Sunyaev-Zel'dovich (SZ) effects, which have become critical tools for: probing structure formation; testing  $\Lambda$ CDM and constraining extensions to it via, for example, determinations of  $\sigma_8$  and the sum of neutrino masses  $\sum m_\nu$  [1–6]; constraining the epoch of reionization [7–9]; detecting high redshift galaxy clusters [10–14]; characterizing the thermodynamics of the hot gas and the impact of astrophysical feedback in galaxy groups [15–18].

However, the small-scale measurements of the CMB are significantly affected by contamination from instrumental noise, diffuse emission from dusty star-forming galaxies – commonly referred to as the cosmic infrared background (CIB) – and radio galaxies. Among these, CIB is particularly challenging to model since the diffuse emission is made up of multiple populations of galaxies over a wide range of redshifts, which contribute differently to each frequency band, introducing significant decorrelations between widely separated instrumental bands [19]. The CIB dominates temperature measurements at arc-minute scales and sets a floor for the current and future CMB temperature measurements [see Figures 1 and 2 of 20, for example].

While polarized CMB, which is relatively free from these contaminants, will be an important channel for future CMB lensing reconstruction, temperature-based CMB lensing will continue to add significant information over the next decade, and will dominate the small-scale lensing measurements in the future [21]. Similarly, robust measurements of small-scale temperature anisotropies will also be crucial for extracting information from kSZ and tSZ signals, and also for cross-correlations with galaxy surveys.

It is therefore essential to develop improved models of these contaminating signals. In particular, it is important to jointly model the lensing, SZ, and CIB signals using correlated simulations of the extragalactic sky. Over the last few years, a few groups have produced correlated multi-tracer simulations [21–23]. These simulations rely on high-resolution  $N$ -body simulations and ray-tracing, both of which are computationally expensive. As a result, producing on the order of thousands of such simulations is impractical and beyond the scope of any work in the near future.

Recently, several groups have successfully applied generative machine learning techniques for a wide range of astrophysical applications such as: generating correlated extragalactic foregrounds using Generative Adversarial Networks [24] and Normalizing Flows [25], reconstructing non-Gaussian CMB lensing maps [26], denoising weak lensing mass maps [27], and modeling dark matter and interstellar dust fields [28]. In this work, we use the Denoising Diffusion Probabilistic Model framework (DDPMs) [29–31] to synthesize realistic samples of CIB and tSZ at 150 GHz consistent with the Agora simulations. Using beyond-power spectrum statistics, specifically the one-point PDF, the collapsed bispectrum and trispectrum statistics, and the Minkowski functionals, we demonstrate that our generated maps accurately reproduce the non-Gaussian statistics of the Agora simulations. Furthermore, we show that our method can jointly model CIB and tSZ fields, enabling consistent generation of physically correlated map pairs. While this work was in its final stages, Aoyama *et al.* [27] published a similar work using the diffusion model framework to produce galaxy weak-lensing observables.

This paper is organized as follows. In §2, we describe the Agora simulations of extragalactic foregrounds, focusing on CIB and tSZ maps at 150 GHz processed with point-source masking, and low-pass filtering. We detail the conversion of full-sky maps to  $6^\circ \times 6^\circ$  patches for training, including data augmentation and normalization strategies. In §3, we introduce the DDPM framework for generating simultaneous realizations of CIB and tSZ maps by learning their joint non-Gaussian distribution. In §4, we demonstrate the performance of our model in reproducing key non-Gaussian features. We discuss the applications of DDPMs in extragalactic foreground modeling, alongside its limitations in §5 and finally conclude in §6.

## 2 Data

### 2.1 Agora simulations

The Agora suite of simulations [23] provides a coherent framework for modeling correlated extragalactic foreground and secondary CMB anisotropies. The suite includes simulations of CMB lensing, thermal and kinetic Sunyaev-Zel’dovich (tSZ/kSZ) effects, cosmic infrared background (CIB), and radio galaxies, all implemented within a unified lightcone. The simulations are produced by integrating dark matter halos and particles from the MULTIDARK-PLANCK2 (MDPL2, Klypin *et al.* 32)  $N$ -body simulation. Agora [23] self-consistently captures correlations between different observables, which is essential for studying biases in CMB lensing [20, 33–37], kSZ [9], and cross-correlations of these secondaries anisotropies with other tracers of large-scale structures [38, 39].

In this work, we focus on two foreground signals, CIB and tSZ, that pose serious challenges for cosmological inferences such as CMB lensing, kSZ, and small-scale CMB temperature power spectrum analyses. The CIB and tSZ are non-Gaussian and also correlated with each other. This choice allows us to evaluate the performance of DDPMs on correlated, highly non-Gaussian extragalactic foregrounds before extending to more complex combinations. Throughout this work, we work with the simulated maps from Agora centered at the 150 GHz band using a bandpass similar to the South Pole Telescope SPT-3G experiment [40]. Agora’s tSZ signal map is generated by pasting halo profiles, calibrated using BAHAMAS hydrodynamical simulation [41, 42], at the halo locations. The CIB signal map is produced by assigning stellar mass and star formation rate for each halo using the UNIVERSEMACHINE [43] code.

We use Agora’s CIB and tSZ simulations to generate both the training and validation samples. To this end, we extract a number of  $6^\circ \times 6^\circ$  sky patches with  $1.40625'$  pixels from the full-sky HEALPix [44] map. We also apply a random rotation and flip to each patch to increase the number of training patches. While such augmentations introduce some correlation between derived samples, they still provide additional examples of localized structures in varying orientations, which improves model generalization without significantly biasing the learned statistical properties. The sky patches are split into 80% for DDPM training and 20% for validation. We normalize the pixel intensities to  $[0,1]$  to stabilize training. However, unlike discriminative models, diffusion models do not rely on validation or test sets for early stopping or model selection, as their evaluation typically involves generating samples and comparing distribution-level statistics.

Before extracting the sky patches, we also apply the following to the full-sky CIB and tSZ maps.

- **Point Source Masking:** We mask sources brighter than 2 mJy using a single-pixel mask. This threshold roughly corresponds to  $10\sigma$  detections in upcoming experiments [45]. The masked pixels are set to zero, and the overall sky fraction removed is less than 1%. While single-pixel masking is not realistic for actual data, note that the simulations used for DDPM training do not have an experimental beam and hence using a single pixel is sufficient for masking the source signal.
- **Cluster Masking:** We mask locations of clusters with mass  $M_{500c} \geq 3 \times 10^{14}$ , approximately corresponding to  $\sim 10\sigma$  detections for upcoming CMB surveys [46]. Unlike point sources, the signal from galaxy clusters is not contained within a single pixel. We therefore apply circular masks with radii ranging from  $3\theta_{500c}$  to  $5\theta_{500c}$  depending on



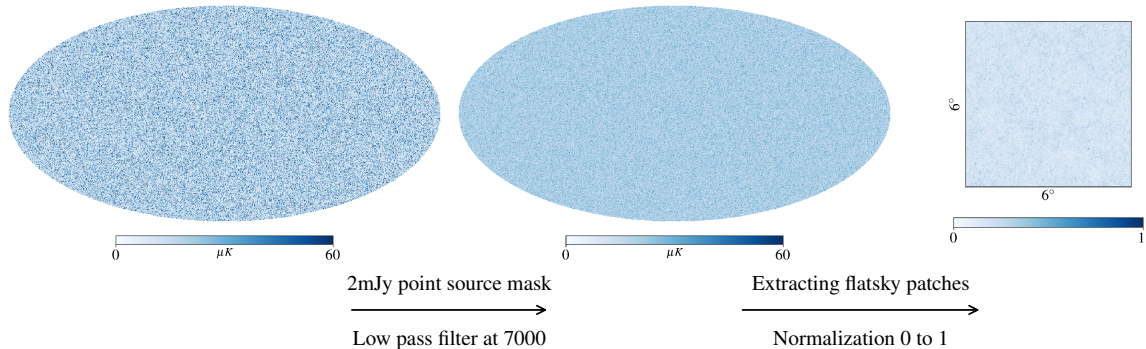


**Figure 1.** Schematic flowchart illustrating the processing pipeline of a full-sky CIB map. The original full-sky CIB map (left) is first processed by applying a 2 mJy point source mask and a low pass filter at 7000, yielding a filtered full-sky map. Subsequently,  $6^\circ \times 6^\circ$  patches are extracted from this processed map and min-max normalized to a range of 0 to 1.

the cluster mass, with a minimum masking radius set to  $10'$ . While this is an extremely conservative masking, the mask only removes  $\sim 3 - 4\%$  of the sky fraction, and thus we do not modify it further. Masked regions are inpainted with Gaussian random values with a mean and standard deviation corresponding to the entire map. In the above equation for the masking radius,  $\theta_{500c}$  corresponds to the angular extent of the cluster defined as  $\theta_{500c} = R_{500c}/D_A$  where  $R_{500c}$ , expressed in Mpc, is the physical radius of the cluster at which the mass density is 500 times the critical density of the Universe at the cluster redshift  $z$  and  $D_A$  is the angular diameter distance to redshift  $z$  in Mpc.

- **Low-pass filtering:** Finally, we low-pass filter the simulations to remove aliasing artifacts from scales  $\ell \geq 7000$  while extracting the patches.

### 3 Methodology

#### 3.1 DDPM Framework

Denoising Diffusion Probabilistic Models are a class of generative models that can learn complex data distributions and generate new samples from the learned distribution. Typically, a DDPM contains two processes: a **Forward process** which iteratively perturbs a highly structured data sample and gradually adds random noise over many steps, destroying the original structure; and a **Reverse process** that then learns to restore structure in the data by removing noise iteratively. Reversing such an entropy-increasing process normally requires an external influence, which in this case is provided by a neural network that encodes information about the structures and correlations present in the original data distribution. The reverse process can be seen as a time-reversed stochastic differential equation (SDE), where the neural network applies a time-dependent drift proportional to the score function ( $\nabla \log p(\mathbf{x})$ ). Learning this score field is the essential core of DDPMs.

**Forward Process** Let  $\mathbf{x}_0$  be a data sample from the true distribution. The forward process defines a Markov chain that gradually perturbs  $\mathbf{x}_0$  into standard Gaussian noise over  $T$  steps with a fixed variance schedule.

$$q(\mathbf{x}_{1:T} | \mathbf{x}_0) := \prod_{t=1}^T q(\mathbf{x}_t | \mathbf{x}_{t-1}), \quad q(\mathbf{x}_t | \mathbf{x}_{t-1}) := \mathcal{N}(\mathbf{x}_t; \sqrt{1 - \beta_t} \mathbf{x}_{t-1}, \beta_t \mathbf{I})$$

One can check that this formulation ensures that after long enough time, the final state  $\mathbf{x}_T$  tends to a standard Gaussian distribution. We use  $T = 1000$  timesteps with a sigmoid schedule  $\beta_t$  ranging from  $\beta_1 = 10^{-4}$  to  $\beta_{1000} = 0.02$ .

**Reverse process** The reverse process is modeled by a neural network trained to approximate the distribution:

$$p_\theta(\mathbf{x}_{t-1} | \mathbf{x}_t) = \mathcal{N}(\mu_\theta(\mathbf{x}_t, t), \beta_t),$$

Our DDPM builds on the architecture of Wang [47]<sup>1</sup>, which uses a U-net [48] architecture with self-attention mechanisms for the reverse process. U-Net is a convolutional neural network well-suited for image-to-image tasks. The U-net architecture consists of two major components: an *Encoder* (contracting path) and a *Decoder* (expanding path). The contracting path reduces the spatial resolution of the input images while capturing increasingly abstract features through a series of convolutional and downsampling operations. This allows the network to learn global context and structures. The expanding path then upsamples these features back to the original resolution, using transpose convolution layers. Crucially, the U-net also consists of *skip connections* between the encoder and decoder blocks that allow fine-scale spatial information to be reintroduced during upsampling. This enables the network to localize and reconstruct fine-scale features, allowing for the recovery of small-scale features present in maps of CIB and tSZ. In our DDPM, we employ a series of four downsampling/upsampling blocks, and incorporate self-attention [49] modules at intermediate resolutions to better capture long-range dependencies such as clustering.

Directly optimizing the log-likelihood,  $\sum_{i=1}^n \log p_\theta(\mathbf{x}_0^{(i)})$ , where  $\mathbf{x}_0^{(1)}, \dots, \mathbf{x}_0^{(n)}$  are the samples from  $\mathbf{x}_0$ , is intractable due to the complexity of marginalizing over all possible diffusion trajectories, which requires integrating over the full sequence of latent variables,  $\mathbf{x}_{1:T}$ . Instead, we train the model by maximizing a lower bound on the negative log likelihood, known as the variational lower bound (VLB) or evidence lower bound (ELBO) as done in Ho *et al.* [Eq. 3 of 30]. The model is trained by minimizing an empirical estimate of this objective. Note that the objective does not directly incorporate any of the summary statistics described below.

### 3.2 Summary Statistics

We evaluate the fidelity of our trained model by using three sets of samples: hold-out patches from the Agora simulation, DDPM-generated samples, and patches from a Gaussian realization constructed to match the auto-power spectra of the CIB and tSZ as well as their cross-power spectrum. These Gaussian patches serve as a baseline for assessing the ability to capture non-Gaussian features beyond the two-point function.

To quantify the statistical precision expected in future experiments, we add S4-Ultra deep-like internal linear combination (ILC) residual noise based on Raghunathan and Omori [20] to both Agora and DDPM samples. This noise is included only when computing the

<sup>1</sup><https://github.com/lucidrains/denoising-diffusion-pytorch>

variance (not the mean), allowing for an estimate of expected uncertainty without requiring explicit noise debiasing.

The first point of comparison is the angular power spectrum, which quantifies scale-dependent correlations in the maps. We compute it using a binned flat-sky power spectrum estimator over a range of  $300 < \ell < 4000$ , in bins of width  $\Delta\ell = 60$ . For the DDPM-generated samples, we initially observe a slight deficit in the power spectrum amplitude, dominant in the Poisson part of the power spectrum. We attribute this to the difficulty of capturing rare, high-intensity pixels—an established limitation of diffusion models [50]. To mitigate this, we apply a post-training rescaling of the pixel intensities. Specifically, we multiply each DDPM sample by a single global factor: the ratio of the standard deviation of all the Agora samples to that of all the generated samples. For the CIB maps, we find a rescaling factor of 1.0328, while for the tSZ maps, we obtain 1.1425. This post-training adjustment proves remarkably effective: it restores agreement with the target power spectrum and also substantially improves the performance of the model across all subsequent summary statistics, without having to retrain the model.

The more interesting metrics are those that quantify the correlations beyond the power spectrum. We looked at several benchmarks of non-Gaussianity, including physically motivated statistics like the bispectrum and the trispectrum, which are sensitive to lensing-induced mode coupling but are expensive to compute. We also examine more traditional measures such as the Minkowski functionals and normalized pixel intensity histograms. We discuss each of them below.

- (1) **Pixel Intensity Histograms:** Normalized histograms of pixel values probe the one-point probability density function (PDF). We compute normalized histograms for 200 samples of CIB and tSZ from test samples and DDPM generated samples. The histograms are constructed using 1000 bins over a range  $[0 \mu K, 100 \mu K]$  for CIB and  $[-100 \mu K, 0 \mu K]$  for tSZ. The histograms are smoothed using a Gaussian kernel with  $\sigma = 1$  to suppress noise.
- (2) **Minkowski Functionals:** Minkowski Functionals [51] characterize the morphology of excursion sets – defined as the pixels with intensities above a certain threshold  $\nu$ . Typically, there are three functionals defined:  $M_0(\nu)$ : Area fraction (cumulative distribution function),  $M_1(\nu)$ : Total boundary length of excursion sets, and  $M_2(\nu)$ : Euler characteristic (number of connected components minus holes), across a range of intensity thresholds  $\nu$ . We use the Boelens and Tchelepi [52] software package to compute these quantities for threshold intensities  $\nu \in [0, 1]$  on normalized maps.
- (3) **Bispectrum and Trispectrum:** Although one could compare all higher-order moments, the three-point (bispectrum) and four-point (trispectrum) correlation functions are the most important for lensing analyses. For computational efficiency, we restrict our analysis to the equilateral configurations of the bispectrum and trispectrum which can be estimated from the skewness and kurtosis of the harmonic band-filtered maps, as done in Lee *et al.* [53]. We compute these moments for the sum of CIB, tSZ, and S4-Ultra deep-like noise. We also evaluate these moments individually for CIB and tSZ as well as their cross moments, which can be found in Appendix C. We demonstrate the ability of DDPMs to accurately capture these moments by comparing to Gaussian samples where we expect these moments to be consistent with zero.

## 4 Results

We present the DDPM-based simulations in this section and compare them to the original Agora simulations. We start with basic visual inspections in § 4.1 and then compare the tSZ profiles of haloes between the two simulations using a stacking approach. Next, we perform thorough quantitative comparisons using the summary statistics described above in § 3.2. These include the power spectra comparisons, and also the ones that capture the non-Gaussianity in the data such as the pixel intensity histograms, Minkowski functionals, and higher-order correlation functions, namely the bispectrum and the trispectrum.

### 4.1 Visual Inspection

As a preliminary check, we examine a few randomly selected CIB-tSZ patch pairs from the Agora simulation and compare them to samples generated by the trained DDPM in Figure 2. Visually, the DDPM samples are nearly indistinguishable from the Agora patches; without labels it would be difficult to tell them apart. The DDPM faithfully reproduces large circular cluster masks with similar morphology and statistical properties. It also captures isolated bright pixels corresponding to point sources in both CIB and tSZ maps, appearing at frequencies consistent with the training data. Due to the low-pass filtering applied during preprocessing, these sources sometimes produce characteristic ringing artifacts in their vicinity. The DDPM-generated samples also show similar bright spots with surrounding ripples akin to those present in the Agora patches.

### 4.2 Stacked tSZ profiles

Besides the visual inspections mentioned above, we compare the profiles of the tSZ signals from DDPM with Agora. To this end, we use the tSZ simulations and extract  $31' \times 31'$  cutouts centered at the locations of pixels  $i$  that fall within a given SNR threshold (A,B) defined as  $A\sigma_T < |T_i - \bar{T}| \leq B\sigma_T$ , where  $\bar{T}$  and  $\sigma_T$  represent the mean and the standard deviation of the simulated tSZ map. Specifically, we pick regions in the following SNR ranges: (a)  $5 - 10\sigma$ , (b)  $10 - 20\sigma$ , and (c)  $\geq 20\sigma$ . Note that the simulated maps are free from instrumental noise, and hence the noise corresponds to the tSZ-confusion noise [46] from the other haloes present in the map. The number of haloes picked from Agora and DDPM simulations agree within 5-10% for the first two cases, but the difference is slightly higher ( $\sim 19\%$ ) for the high SNR case. The larger discrepancy for the high SNR case arises from the difficulty in properly capturing the statistics of the massive clusters with the patch size used for training. We discuss this further in the subsequent sections. Once we collect the cutouts of haloes, we compute the stack in each SNR bin as

$$\hat{S}(\theta_x, \theta_y) = \frac{\sum_i w_i S_i(\theta_x, \theta_y)}{\sum_i w_i} \quad (4.1)$$

where the index  $i$  runs over all the clusters in a given SNR bin defined above and we apply uniform weights  $w$  for all the clusters. Here,  $\theta_x$  and  $\theta_y$  are Cartesian angular coordinates with the origin at the cluster center. In Figure 3, we present the radial profile of the stacked tSZ signals,  $\hat{S}(\theta_x, \theta_y)$ , as a function of radius  $\theta = \sqrt{\theta_x^2 + \theta_y^2}$  from the cluster center. To compute the radial profile, we average the stacked map  $\hat{S}(\theta_x, \theta_y)$  over all pixels with coordinates  $(\theta_x, \theta_y)$  such that  $\sqrt{\theta_x^2 + \theta_y^2} \in (\theta_b, \theta_b + \Delta\theta)$ , where  $(\theta_b, \Delta\theta)$  define the edges of the radial bin. We use 10 linearly spaced bins with  $\Delta\theta = 1'$  and  $\theta_{\max} = 10'$ . In the figure, black corresponds to the



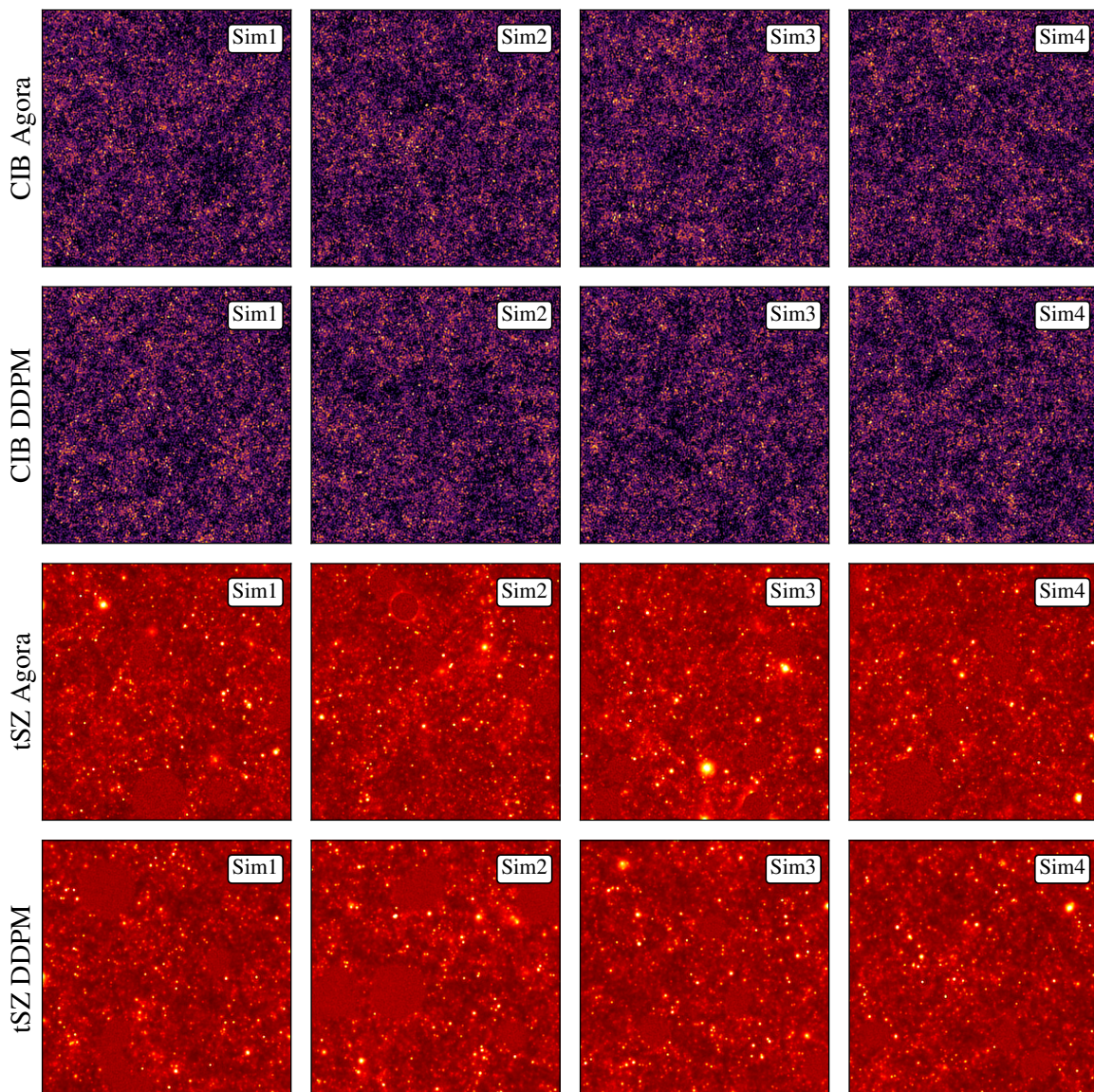


**Figure 2.** Randomly selected patches of the CIB (top two rows) and tSZ (bottom two rows) at 150 GHz. Each column shows a different simulation index. The first and third rows show samples from the Agora simulation, while the second and fourth rows show corresponding outputs from the DDPM. The DDPM closely matches the visual appearance of the training data, reproducing cluster masks, point sources, and even characteristic ringing artifacts from low-pass filtering.

radial profile from Agora and blue corresponds to DDPM simulations. In the top panels, we also show the difference between Agora and DDPM in yellow, and in the bottom panels, we present the ratio. As evident from the figure, radial profile of the tSZ signals from DDPM agrees with the ones from Agora to within 8%. We also note that the radial profiles from both Agora and DDPM simulations do not reach zero even at  $\theta \geq 10'$  from the cluster center. This is due to the 2-halo term of the tSZ signal [54] dominating over the 1-halo term at larger distances from the cluster center, and it is being reproduced in DDPM simulations to within

5% when compared to Agora.

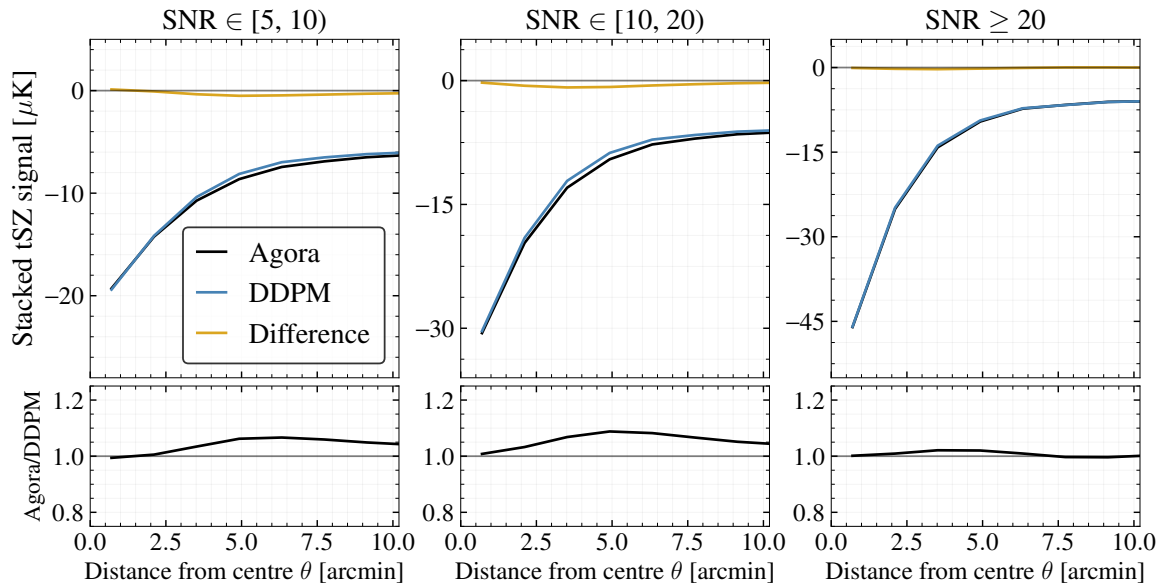


**Figure 3.** Radial profiles of stacked tSZ signals in three SNR bins. The black curves correspond to Agora and the blue to DDPM simulations. We stack roughly 260,000 in the first SNR bin  $\in [5, 10)$ ; 60,000 in the second bin  $\in [10, 20)$ ; and 3,900 in the third bin  $\text{SNR} \geq 20$ . In the top panels, we show the difference between Agora and DDPM profiles in yellow, and present the ratio of the two as a function of distance from the center in the bottom panels. We find that the DDPM simulations agree with Agora simulations to within 8%. In the top panels, the profiles do not reach zero even at larger radii because of the 2-halo term.

### 4.3 Power Spectra comparison

Next, we evaluate the auto- and cross- angular power spectra of 200 randomly selected CIB and tSZ patch pairs generated by the DDPM and compare them to patches from the Agora simulation. The results of this comparison are shown in Figure 4. The CIB exhibits a Poisson-dominated spectrum, where  $D_\ell$  increases as  $\ell^2$ , consistent with a model with Poissonian shot noise term and a continuous clustering term [55]. In contrast, tSZ shows a peak structure due to the characteristic angular size of galaxy clusters, set by their halo pressure profiles. After applying variance rescaling as described in Section 3.2 to the DDPM outputs, to match the true variance, we find that the generated power spectra match the ground truth within 25% of the sample variance across all multipoles. We find that the CIB power spectrum matches well even without rescaling, while the tSZ spectrum requires rescaling to correct for the underestimation of its extreme-valued pixels. The cross-spectrum between the CIB and tSZ, which probes the spatial correlation between dusty star-forming galaxies and the hot gas traced by tSZ, is also successfully reproduced by the DDPM, well within the expected sample variance.

### 4.4 Pixel Intensity Histograms

Figure 5 presents the pixel intensity distributions for the CIB and tSZ maps. The DDPM-generated maps (dashed lines) closely follow the distributions of the Agora simulations (solid

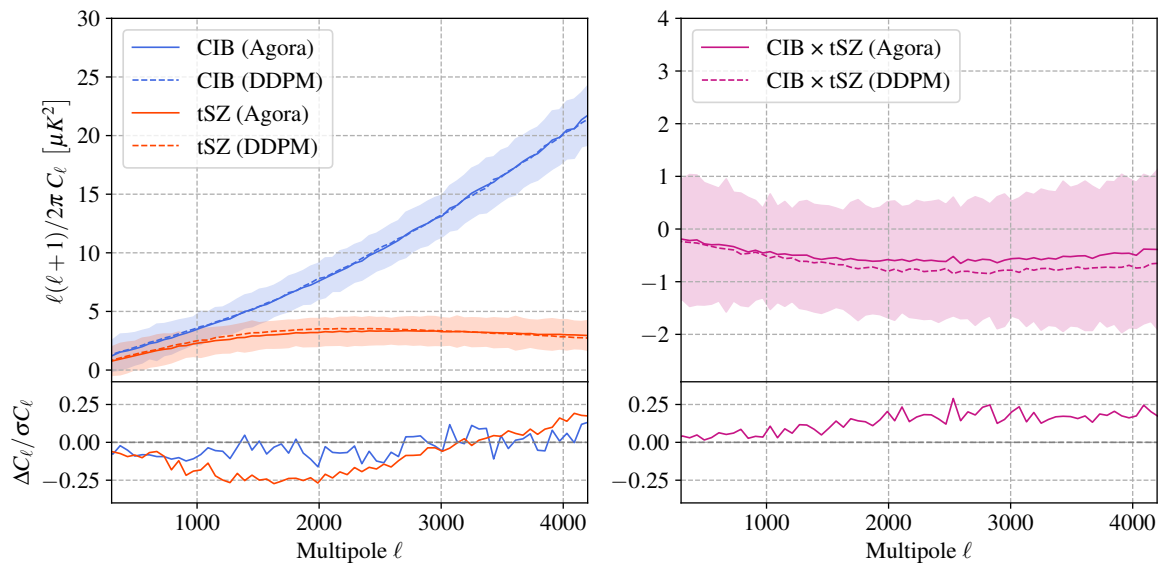


**Figure 4.** Comparison of angular power spectra between DDPM samples and test maps for both auto- and cross-correlations. In the top panel, the auto-power spectra  $C_\ell$  for the CIB and tSZ components (blue and orange, respectively) and the cross-power spectrum  $C_\ell^{\text{CIB} \times \text{tSZ}}$  (pink) are shown for both DDPM (solid lines) and test samples (dashed lines), across multipoles  $\ell = 300\text{--}4200$ . Shaded bands represent the  $1\sigma$  sample variance from the test set. In the bottom panel, residuals between the test and DDPM power spectra, expressed as  $(C_\ell^{\text{Agora}} - C_\ell^{\text{DDPM}})/\sigma(C_\ell^{\text{Agora}})$  are shown.

lines), especially near the mode. This confirms that the diffusion model successfully captures the bulk of the one-point statistics across both components.

However, there are discrepancies present in the distribution tails. For the CIB, we observe a slight underproduction of high-intensity pixels, with a mild shortfall beyond intensities of  $\sim 60 \mu\text{K}$ . For the tSZ, the DDPM underestimates the occurrence of strong decrements (large negative values), which correspond to massive clusters, as seen by the suppressed tails in the unscaled DDPM pixel histogram. These deviations highlight the challenge in recovering rare, high-amplitude fluctuations that drive the heavy tails of these distributions.

#### 4.5 Minkowski Functionals

Figure 6 shows the Minkowski functionals  $M_0$ ,  $M_1$ , and  $M_2$  as a function of threshold  $\nu$  for both the CIB (left) and tSZ (right) maps. The DDPM samples (blue) closely match the real Agora data (black) across all three statistics, demonstrating the model’s ability to reproduce both global and topological features of the fields. For the tSZ channel, there is a small mismatch between the DDPM and Agora curves in  $M_1$  and  $M_2$ , particularly near high-threshold regions where signal is sparse. However, these deviations are minor compared to the significant differences observed with the Gaussian simulations (orange). The Gaussian maps fail to capture the heavy tails and non-Gaussian features present in the real and DDPM-generated maps, resulting in smooth, symmetric  $M_1, M_2$  curves centered at 0.5.



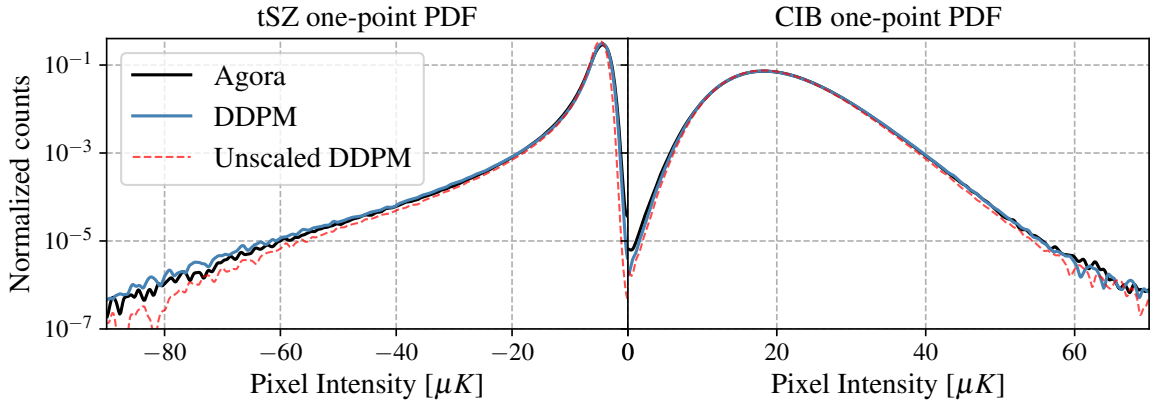


**Figure 5.** Comparison of one-point PDF: Pixel intensity density estimates for test samples (black) and DDPM samples (blue) using histograms. The pixel values were binned into linearly spaced bins, and the normalized histograms are smoothed with a 1D Gaussian filter ( $\sigma = 1$ ) to suppress the high frequency fluctuations near the tails.

#### 4.6 Bispectrum and Trispectrum

In Figure 7, we present the estimated collapsed equilateral bispectrum ( $S_3$ ) and trispectrum ( $S_4$ ) of the sum of CIB, tSZ, and S4-Ultra deep-like instrumental noise, evaluated across a range of harmonic band centers  $\ell_c$ . We compare the results from Agora simulations, DDPM samples, and Gaussian realizations. As expected, the Gaussian samples remain consistent with zero across all  $\ell_c$ , serving as a baseline. The DDPM successfully recovers the non-zero skewness and kurtosis associated with the foregrounds in the Agora simulations. However, minor differences are present between the trispectrum of Agora and the DDPM generated samples at low multipoles. A more detailed breakdown of third- and fourth-order auto- and cross-moments between the CIB and tSZ components, under SPT-3G, S4-Wide, and S4-Ultra deep noise levels, is provided in Appendix C.

We investigated if the underproduction of extreme-value pixels could be the source of the large-scale discrepancy between Agora and DDPM. To this end, similar to the stacking exercise in § 4.2, we select pixel locations satisfying with  $\text{SNR} \geq 10\sigma$ , corresponding to the extreme-value pixels, and use a 2D Gaussian fitting approach to determine the size of the haloes. Next, we mask the locations of these high SNR signals in both Agora and DDPM, and recalculate the bispectrum and trispectrum statistics. While masking these extreme signals reduces the non-Gaussianities suppressing both the bispectrum and the trispectrum, it does not have a noticeable impact on the differences between Agora and DDPM. It is important to note here that we do not retrain the DDPM after masking the extreme-value pixels and leave a more careful investigation of this discrepancy to a future work.

## 5 Discussion

In this section, we discuss some of the applications we envision for DDPMs in extragalactic foreground modeling, outline some practical challenges to their deployment in analysis pipelines, and compare DDPMs with other generative modeling approaches.

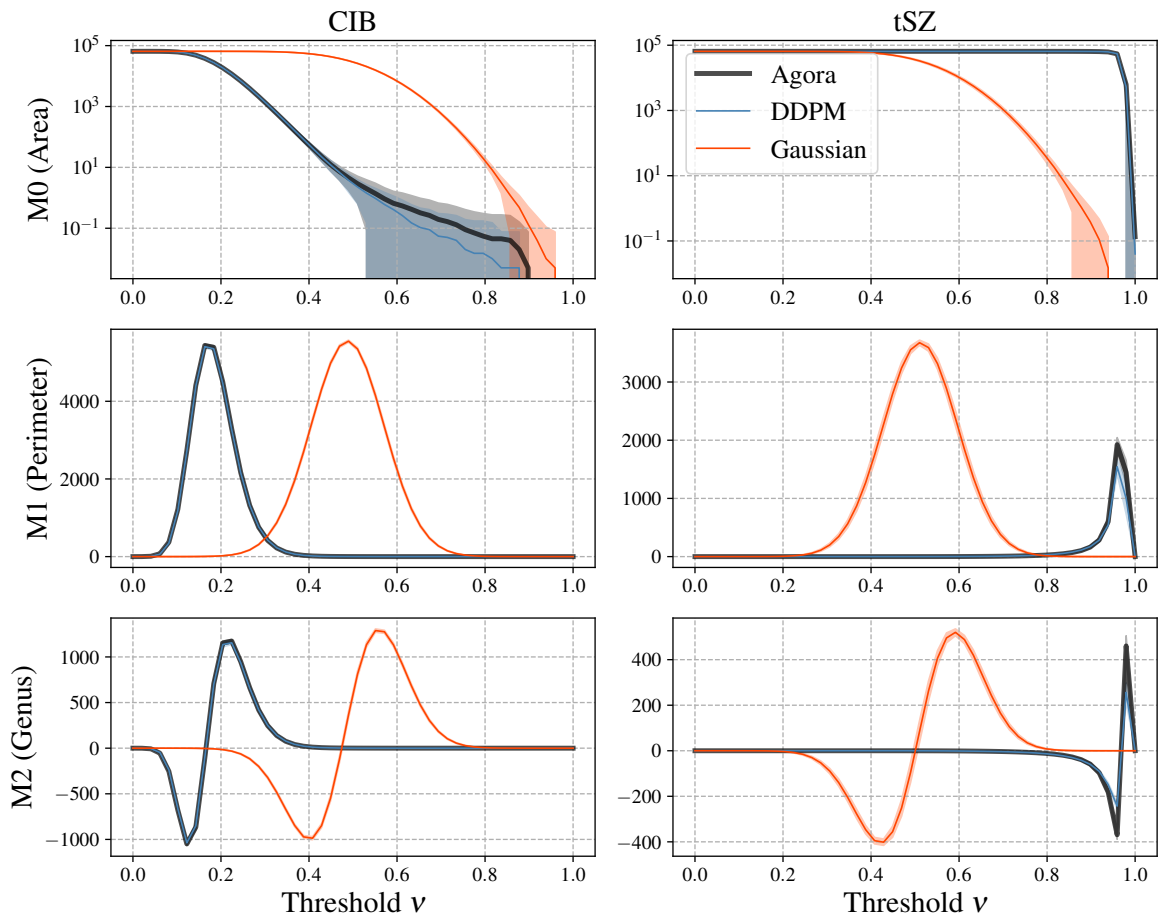


**Figure 6.** Minkowski functionals  $M_0$  (Area),  $M_1$  (Perimeter), and  $M_2$  (Genus) as a function of intensity threshold  $\nu$  for cosmic infrared background (CIB, left) and thermal Sunyaev-Zel’dovich effect (tSZ, right). We compare real maps from Agora (black), DDPM-generated samples (blue), and Gaussian simulations (orange). Shaded regions denote standard deviations across realizations.

## 5.1 Applications

We imagine two primary applications for DDPMs in CMB analysis: (1) as a rapid generator of simulations that can be used in downstream analysis pipelines, and (2) as a probabilistic model in a Bayesian inference engine. We discuss them below.

- (1) Correlated multi-tracer simulations such as Agora or Websky rely on computationally expensive  $N$ -body simulations and ray-tracing, and often require several thousands of CPU hours to generate a single realization. DDPMs on the other hand, once trained on a few thousand patches from these simulations, can generate realistic samples with accurate summary statistics in a matter of seconds, as demonstrated in this work. These models can rapidly generate large ensembles of simulations to test for possible biases and to build accurate covariance matrices.
- (2) The trained DDPM can be incorporated into Bayesian inference engines like MUSE [56]. Within such a framework, the DDPM can be used in two ways: either as part

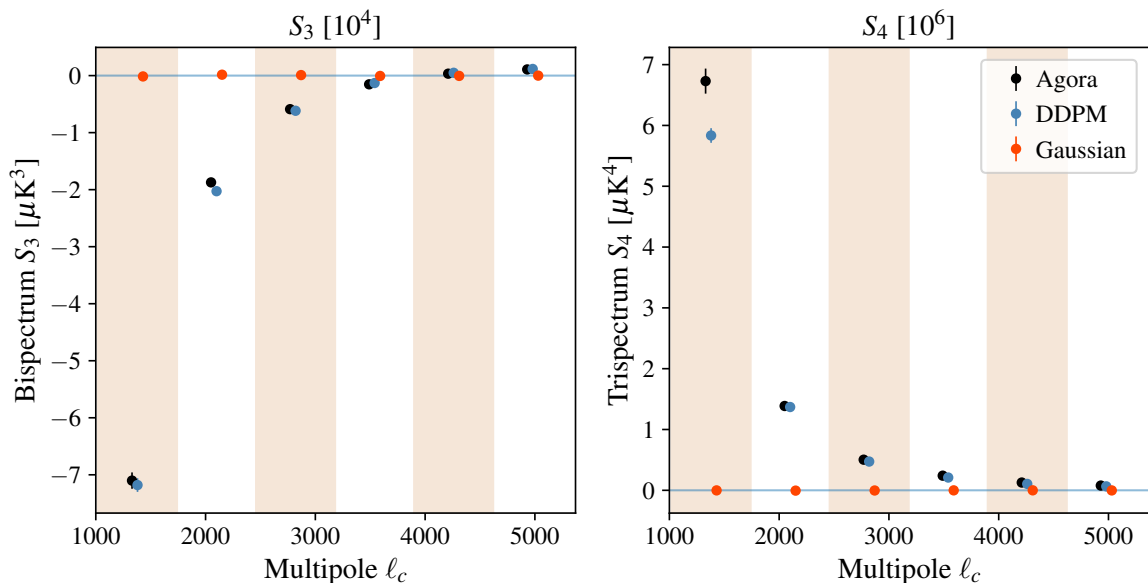


**Figure 7.** Comparison of bispectra and trispectra of the sum of CIB and tSZ signals and noise as a function of band center,  $\ell_c$ . Each panel compares the mean and standard error of the statistics across 800 patches from three models, Gaussian simulations, Agora simulations, and DDPM samples, for S4-Ultra deep-like instrumental noise levels.

of the data model, where it can replace simplistic Gaussian priors with physically motivated, complex foreground distributions, or in the forward simulator, where it generates synthetic skies that propagate through the full pipeline to correct for biases in the inference process.

## 5.2 Real-world challenges

*Increasing the size of the simulations:* Perhaps the most significant challenge in applying DDPMs to real-world analysis tasks is their extension to larger sky areas. The number of available training samples decreases as the patch size increases, since only a handful of correlated multi-tracer simulations currently exist. Moreover, the computational cost of training these models scales typically as  $\mathcal{O}(N_{\text{pix}}^2)$  or higher. In this work, we train on patches of size  $6^\circ \times 6^\circ$ , which lets us extract about 4000 training examples (with data augmentation) from the Agora simulation. This was the largest patch size for which we were able to train a model reliably. We experimented with larger patches of size  $10^\circ \times 10^\circ$ , but observed a significant degradation in sample quality, likely due to insufficient training data. However, most of the current surveys span sky areas at least 10 times larger. Extending DDPMs to generate larger sky areas thus remains a challenge. One promising direction is the Patch Diffusion framework proposed in [57], which we leave for future work.

*Reproducibility of extreme-value pixels:* A consequence of the above limitation in the number of available sky patches for training, is the difficulty in capturing the statistics of extreme-value pixels. In this work, we masked sources brighter than 2 mJy and clusters with mass  $M_{500c} \geq 3 \times 10^{14}$ . Since both the source number counts and the halo mass function are a steep function of the source flux or the cluster mass, the patch size of  $6^\circ \times 6^\circ$  that we use

for training does not have enough high-flux or massive clusters for reliable training. This, however, is not a major obstacle for the current or future cosmological analysis. Note that the power spectrum and CMB lensing analyses require these extreme sources to be either masked or inpainted to avoid the challenges in properly modeling the artifacts due to filtering and biases in lensing at these locations.

*Dependence on the training samples:* Finally, any generative model is only as good as the training data. In this work, we have not attempted to generate a new set of cosmological simulations from scratch but only to increase the number of realizations using existing simulations with the DDPM framework. Our training data comes from the Agora simulation [23] which adopted a specific set of cosmological and astrophysical parameters. Any mismatches between these assumptions and the true sky could lead to biases when the generative model is applied to data. Whether these differences are negligible depends on the specific application. Future work could explore training on an ensemble of simulations with varied physical assumptions, or conditioning on cosmological parameters to marginalize over modeling uncertainties.

### 5.3 Comparison with other generative modeling approaches

Generative models such as Generative Adversarial Networks (GANs), Variational Autoencoders (VAEs), Normalizing Flows, and Denoising Diffusion Probabilistic Models (DDPMs) offer distinct trade-offs for modeling extragalactic foregrounds. GANs have been used to model astrophysical sources, but are notoriously unstable during training due to issues like mode collapse and vanishing gradients [58]. Additionally, GANs do not provide an explicit likelihood [59], limiting their applicability in Bayesian inference frameworks. VAEs provide a more stable training process and offer an explicit likelihood-based framework, making them attractive for Bayesian applications. However, they often rely on simplistic latent variable distributions (e.g., Gaussian), which can result in oversmoothed outputs and loss of angular resolution, which is particularly problematic for fine-scale structures in astrophysical maps [60]. Normalizing Flows allow for exact likelihood estimation and efficient sampling via invertible mappings, but their expressiveness is limited by topological constraints imposed by the choice of priors, especially when modeling multi-modal distributions [61]. DDPMs provide stable training procedures without mode collapse, producing diverse and robust samples without the need for manual intervention or tweaking. DDPMs can preserve the small-scale features present in astrophysical foregrounds, such as the resolved dusty galaxies (CIB) and galaxy clusters (tSZ). Recent comparative studies demonstrate that diffusion models outperform GANs and VAEs in tasks such as denoising weak lensing mass maps and reconstructing non-Gaussian lensing signals. For example, Aoyama *et al.* [27] found that diffusion models achieve more accurate recovery of cosmological statistics across multiple benchmarks, although at the cost of increased training time and memory usage.

## 6 Conclusions

In this work, we have demonstrated the application of Denoising Diffusion Probabilistic Models to synthesize realistic extragalactic foreground maps, focusing on the Cosmic Infrared Background and thermal Sunyaev–Zel’dovich maps at 150 GHz from the Agora suite of simulations. We showed that the DDPM learns the full joint distribution of these signals,

enabling the generation of correlated sky patches that faithfully reproduce not only the two-point (power spectrum) statistics but also higher-order non-Gaussian features such as the bispectrum, trispectrum, pixel intensity distributions, and Minkowski functionals.

While DDPMs produce high-fidelity samples, we identified key challenges in their practical deployment. Notably, rare high-intensity pixels that can contribute significantly to the Poisson part of the power spectrum are underrepresented in the generated maps. This limitation leads to a slight deficit in the amplitude of the generated power spectra. We found that a simple post-hoc variance rescaling of the generated maps effectively corrects this issue, improving agreement across summary statistics. A more significant challenge lies in scaling these models to larger sky areas. The number of available training samples decreases with increasing patch size, since only a handful of correlated multi-tracer simulations currently exist. Additionally, the fidelity of the DDPMs is tied to the quality and assumptions of the training data. Any discrepancies between these assumptions and the true sky could introduce modeling biases. These limitations must be addressed before broader deployment of DDPMs in cosmological analyses.

The DDPM framework naturally generalizes to additional foreground components, and can be extended across multiple frequencies to model full spectral energy distributions. This makes DDPMs a promising tool for forward modeling in CMB pipelines, where fast and accurate simulations are needed for foreground marginalization and unbiased parameter estimation. Physics-based simulations like Agora require thousands of computing hours to produce a single realization, while DDPMs can generate new CIB-tSZ map pairs in seconds. This opens the door to large-scale, rapid generation of realistic foreground realizations, something that has been out of reach with traditional simulation methods. We share our code and the plotting scripts in this [GitHub repo](#)<sup>9</sup>.

## Acknowledgments

We would like to thank Marius Millea for useful discussions and Yuuki Omori for consultation about Agora [23] data products. KP and LK acknowledge the support of Michael and Ester Vaida and the National Science Foundation via award OPP-1852617. SR acknowledges the support by the Illinois Survey Science Fellowship from the Center for AstroPhysical Surveys at the National Center for Supercomputing Applications.

The Agora simulations use the CosmoSim database, which is a service by the Leibniz-Institute for Astrophysics Potsdam (AIP). The MultiDark database was developed in cooperation with the Spanish MultiDark Consolider Project CSD2009-00064.

This work made use of the following computing resources: Illinois Campus Cluster, a computing resource that is operated by the Illinois Campus Cluster Program (ICCP) in conjunction with the National Center for Supercomputing Applications (NCSA) and which is supported by funds from the University of Illinois at Urbana Champaign; the computing resources provided on Crossover, a high-performance computing cluster operated by the Laboratory Computing Resource Center at Argonne National Laboratory; and the National Energy Research Scientific Computing Center (NERSC), a DOE Office of Science User Facility supported by the Office of Science of the U.S. Department of Energy under Contract No. DE-AC02-05CH11231.

## A Training Details

The training dataset comprises roughly  $\sim 4,000$  patches of size  $256 \times 256 \times 2$  (CIB + tSZ channels). We use a U-Net architecture with four encoder and decoder blocks, with channel depths of 64, 128, 256, and 512. The network includes sinusoidal timestep embeddings and self-attention layers at intermediate resolutions. A detailed breakdown of the architecture is provided in Table 1.

Training is carried out over  $T = 1000$  diffusion steps using a sigmoid noise schedule, with  $\beta_1 = 10^{-4}$  and  $\beta_{1000} = 10^{-2}$ . We optimize the velocity-prediction objective as defined in Salimans and Ho [62], using the Adam optimizer [63] with a learning rate of  $1 \times 10^{-4}$  and a batch size of 16. The model is trained for approximately 100,000 steps on a single NVIDIA A100 GPU, with checkpointing enabled. Full training takes around 30 hours. Once trained, sampling takes roughly 1–2 seconds per patch on the same hardware.

Stage	Output ( $H \times W \times C$ )	Key operations
Input conv	$256 \times 256 \times 64$	$7 \times 7$ Conv (stride 1, pad 3)
Time embedding	–	Sinusoidal pos-emb $\rightarrow$ Linear $\rightarrow$ GELU $\rightarrow$ Linear
Down 0	$128 \times 128 \times 64$	$2 \times$ ResNet + LinearAttn + Downsample
Down 1	$64 \times 64 \times 128$	$2 \times$ ResNet + LinearAttn + Downsample
Down 2	$32 \times 32 \times 256$	$2 \times$ ResNet + LinearAttn + Downsample
Down 3	$32 \times 32 \times 512$	$2 \times$ ResNet + Full Attn + $3 \times 3$ Conv
Bottleneck	$32 \times 32 \times 512$	ResNet $\rightarrow$ Full Attn $\rightarrow$ ResNet
Up 3	$64 \times 64 \times 256$	$2 \times$ ResNet + Full Attn + Upsample
Up 2	$128 \times 128 \times 128$	$2 \times$ ResNet + LinearAttn + Upsample
Up 1	$256 \times 256 \times 64$	$2 \times$ ResNet + LinearAttn + Upsample
Up 0	$256 \times 256 \times 64$	$2 \times$ ResNet + LinearAttn + $3 \times 3$ Conv
Final	$256 \times 256 \times 2$	ResNet (skip) + $1 \times 1$ Conv
<b>Total trainable parameters</b>		35.7 M

**Table 1.** U-Net architecture used in this work. Input maps are of shape  $256 \times 256 \times 2$ , representing CIB+tSZ channels. Total trainable parameters: 35.7 million.

## B Correlations across frequency

To assess the ability of DDPMs to capture the inter-frequency correlations, we trained a model to jointly generate CIB maps at 95, 150, and 857 GHz. The CIB fields at 95 and 150 GHz are expected to be highly correlated, while decorrelation becomes apparent at 857 GHz due to the increased contribution from lower-redshift sources. Figure 8 demonstrates that the DDPM successfully reproduces the correlated structures present in the CIB maps across three frequencies. In addition to visual inspection, we quantitatively assess the model’s ability to reproduce the frequency-dependent correlations using angular power spectra. In Figure 9, we show the standard errors between the DDPM and Agora power spectra for all auto- and cross-power spectra for the three frequencies. The errors are generally within 50% of the standard deviation. The right panel shows the cross-correlation coefficients between the 95, 150, and 857 GHz maps. The DDPM captures the near-unity correlation between 95 and 150 GHz and  $\sim 80\%$  (77%) between 150 (95) GHz and 857 GHz, consistent with the Agora



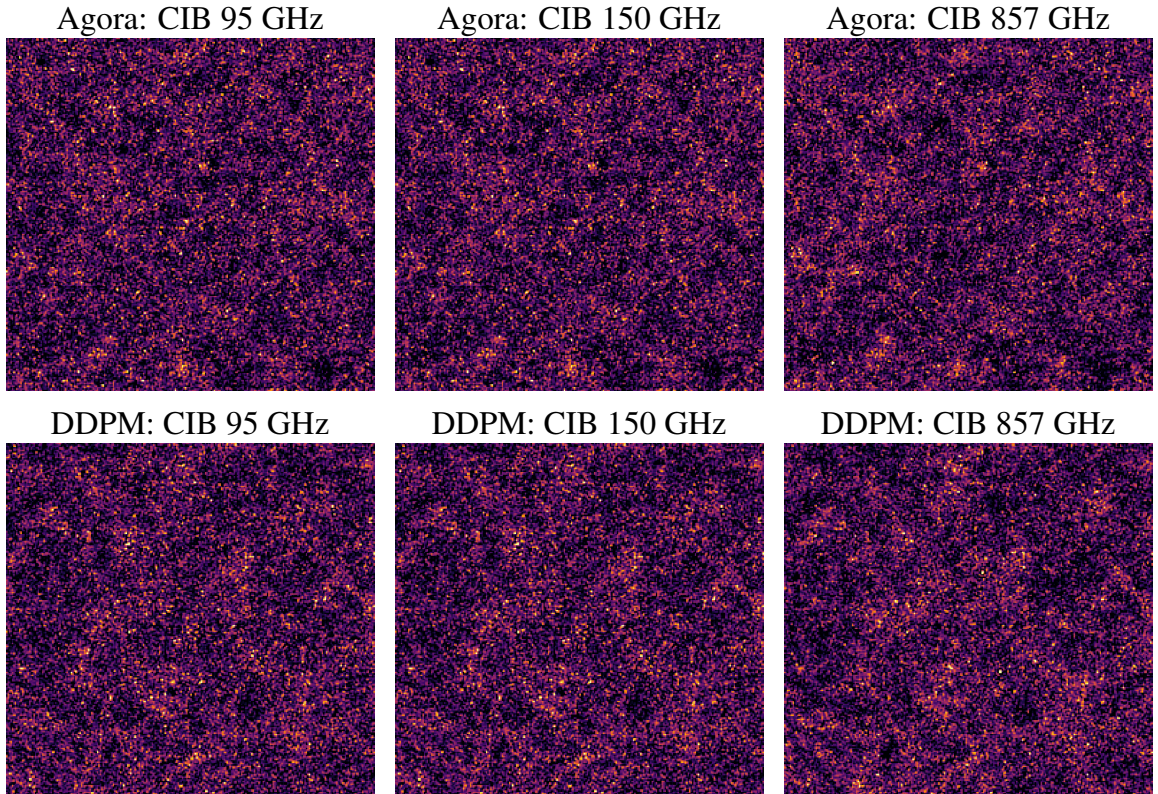


**Figure 8.** Examples of CIB maps at 95, 150, and 857 GHz from the test set (top row) and the DDPM (bottom row). Each row shows the same sky patch across different frequencies. The DDPM-generated maps preserve the highly correlated filamentary structures and small-scale fluctuations present in the Agora simulation. For visualization, each map is standardized by subtracting its mean and dividing by its standard deviation to ensure perceptual consistency across channels.

simulations. We observe that the decorrelation between frequency bands is slightly milder for the DDPM samples at higher multipoles compared to the original Agora simulations. Similar to the investigation done in § 4.6, we mask the extreme-value pixels in the CIB maps and recalculate the correlation coefficients for both Agora and DDPM. The impact of this masking is only marginal and well within the errors shown in Fig. 8. We also defer a careful study of this behavior to a future work.

### C Higher order auto- and cross- moments

In Figure 10 and Figure 11, we show a more detailed version of Figure 7. We present the bispectra and trispectra for CIB-only, tSZ-only, and all possible CIB–tSZ combinations across three noise levels (SPT-3G, S4-Wide, and S4-Ultra deep).

### References

- [1] M. Kaplinghat, L. Knox, and Y.-S. Song, *Phys. Rev. Lett.* **91**, 241301 (2003).
- [2] B. Horowitz and U. Seljak, *MNRAS* **469**, 394 (2017), [arXiv:1609.01850 \[astro-ph.CO\]](https://arxiv.org/abs/1609.01850).



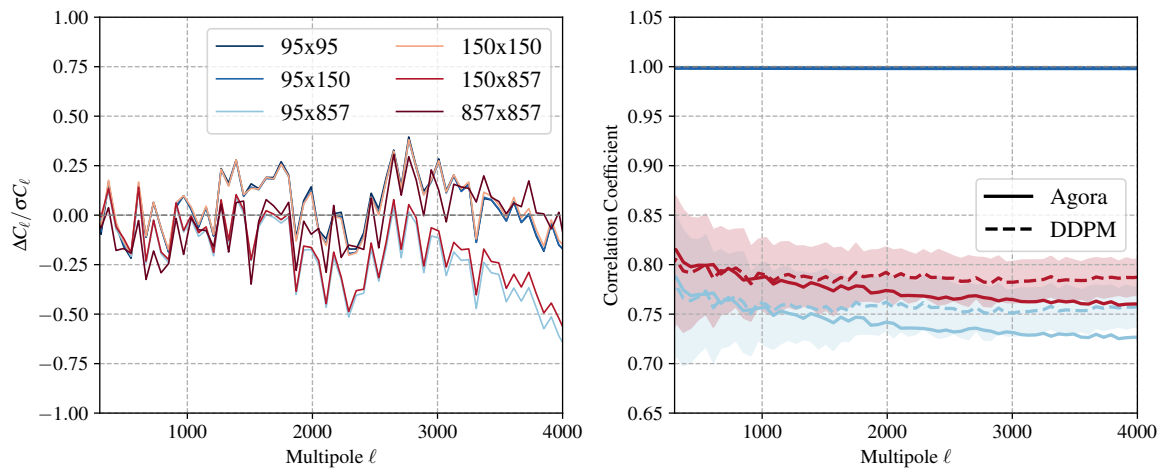


**Figure 9.** *Left panel:* Standard errors of the DDPM power spectra compared to the Agora test set for all auto- and cross-power spectra of the 95, 150, and 857 GHz CIB maps, averaged over 200 samples. The errors in each spectra is generally within 50%. *Right Panel:* Cross-correlation coefficients between different frequency bands computed from the Agora test maps (solid) and DDPM samples (dashed). The DDPM accurately reproduces the correlations observed in the Agora simulations.

- [3] S. Bocquet, S. Grandis, L. E. Bleem, others, (SPT, and DES Collaborations), [Physical Review D \*\*110\*\*, 083510 \(2024\)](#), [arXiv:2401.02075 \[astro-ph.CO\]](#) .
- [4] M. S. Madhavacheril, F. J. Qu, B. D. Sherwin, *et al.*, [arXiv e-prints](#) , [arXiv:2304.05203 \(2023\)](#), [arXiv:2304.05203 \[astro-ph.CO\]](#) .
- [5] F. Ge, M. Millea, E. Camphuis, C. Daley, N. Huang, Y. Omori, W. Quan, *et al.* (SPT-3G Collaboration), [Phys. Rev. D \*\*111\*\*, 083534 \(2025\)](#).
- [6] F. J. Qu, B. D. Sherwin, M. S. Madhavacheril, D. Han, K. T. Crowley, *et al.*, [ApJ \*\*962\*\*, 112 \(2024\)](#), [arXiv:2304.05202 \[astro-ph.CO\]](#) .
- [7] C. L. Reichardt, S. Patil, *et al.*, [ApJ \*\*908\*\*, 199 \(2021\)](#), [arXiv:2002.06197 \[astro-ph.CO\]](#) .
- [8] A. Gorce, S. Ilić, M. Douspis, D. Aubert, and M. Langer, [A&A \*\*640\*\*, A90 \(2020\)](#), [arXiv:2004.06616 \[astro-ph.CO\]](#) .
- [9] S. Raghunathan, P. A. R. Ade, A. J. Anderson, *et al.* (SPT-3G and SPTpol Collaboration), [Phys. Rev. Lett. \*\*133\*\*, 121004 \(2024\)](#).
- [10] L. E. Bleem, B. Stalder, T. de Haan, *et al.*, [ApJS \*\*216\*\*, 27 \(2015\)](#), [arXiv:1409.0850](#) .
- [11] Planck Collaboration, P. A. R. Ade, N. Aghanim, M. Arnaud, *et al.*, [A&A \*\*594\*\*, A24 \(2016\)](#), [arXiv:1502.01597](#) .
- [12] L. E. Bleem, S. Bocquet, B. Stalder, *et al.*, [ApJS \*\*247\*\*, 25 \(2020\)](#), [arXiv:1910.04121 \[astro-ph.CO\]](#) .
- [13] M. Hilton, C. Sifón, S. Naess, *et al.*, [ApJS \*\*253\*\*, 3 \(2021\)](#), [arXiv:2009.11043 \[astro-ph.CO\]](#) .
- [14] K. Kornoelje, L. E. Bleem, E. S. Rykoff, *et al.*, [arXiv e-prints](#) , [arXiv:2503.17271 \(2025\)](#), [arXiv:2503.17271 \[astro-ph.CO\]](#) .
- [15] E. Schaan, S. Ferraro, S. Amodeo, *et al.*, [Physical Review D \*\*103\*\*, 063513 \(2021\)](#), [arXiv:2009.05557 \[astro-ph.CO\]](#) .

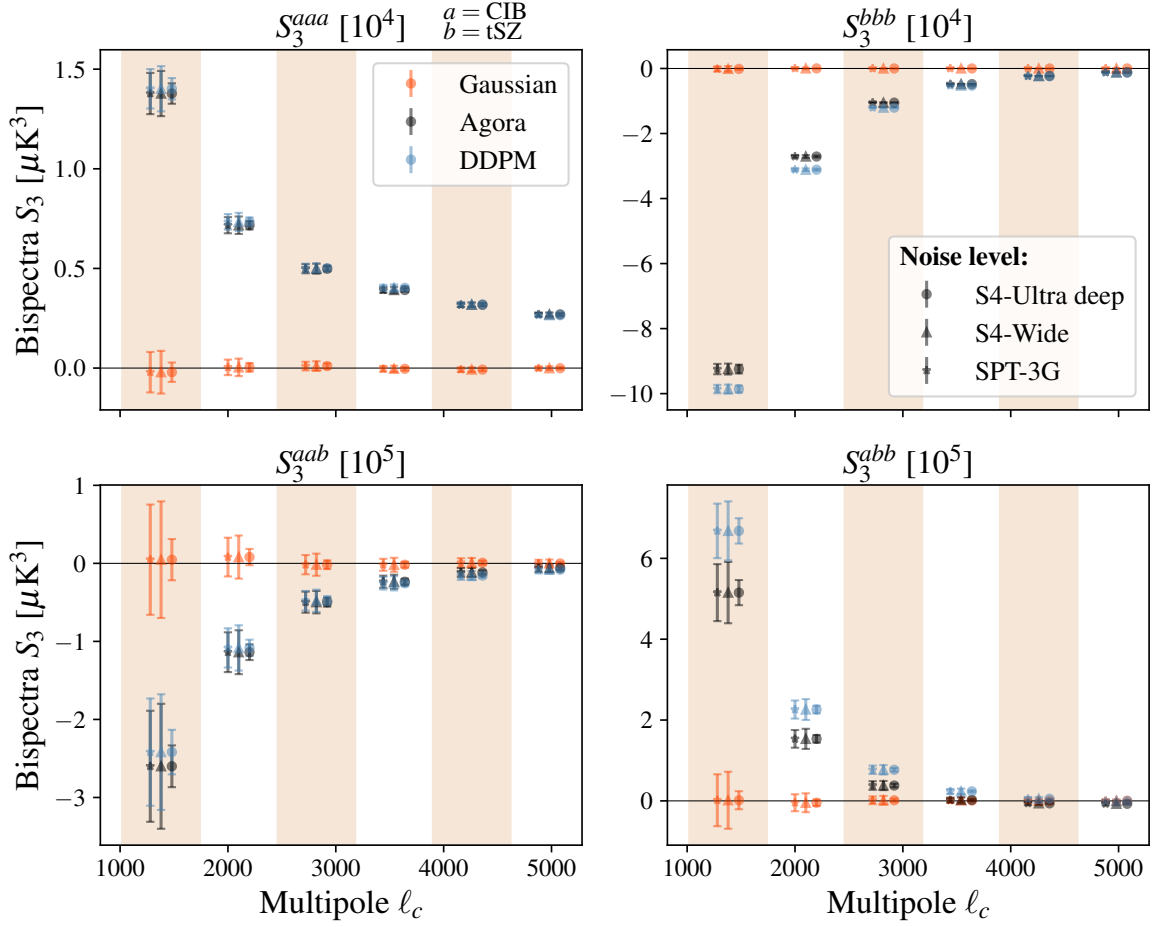


**Figure 10.** Joint bispectrum ( $S_3$ ) statistics of CIB and tSZ maps computed from 800 patches of Gaussian, Agora, and DDPM samples. Each panel shows  $S_3$  for different channel combinations: CIB-only ( $S^{aaa}$ ), tSZ-only ( $S^{bbb}$ ), and cross terms (e.g.,  $S^{aab}$  indicates two CIB and one tSZ input). Error bars denote the standard error across realizations under three instrumental noise levels: SPT-3G, S4-Wide, and S4-Ultra deep. Alternating shaded regions indicate multipole bands used for moment computation.

- [16] L. Bigwood, A. Amon, A. Schneider, *et al.*, *MNRAS* **534**, 655 (2024), [arXiv:2404.06098 \[astro-ph.CO\]](#).
- [17] B. Hadzhiyska, S. Ferraro, B. Ried Guachalla, *et al.*, [arXiv e-prints](#), [arXiv:2407.07152 \(2024\)](#), [arXiv:2407.07152 \[astro-ph.CO\]](#).
- [18] B. Ried Guachalla, E. Schaan, B. Hadzhiyska, *et al.*, [arXiv e-prints](#), [arXiv:2503.19870 \(2025\)](#), [arXiv:2503.19870 \[astro-ph.GA\]](#).
- [19] M. P. Viero, C. L. Reichardt, B. A. Benson, *et al.*, *The Astrophysical Journal* **881**, 96 (2019).
- [20] S. Raghunathan and Y. Omori, *ApJ* **954**, 83 (2023), [arXiv:2304.09166 \[astro-ph.CO\]](#).
- [21] N. Sehgal, S. Aiola, Y. Akrami, *et al.*, in *Bulletin of the American Astronomical Society*, Vol. 51 (2019) p. 6, [arXiv:1906.10134 \[astro-ph.CO\]](#).
- [22] G. Stein, M. A. Alvarez, J. R. Bond, A. v. Engelen, and N. Battaglia, *Journal of Cosmology*

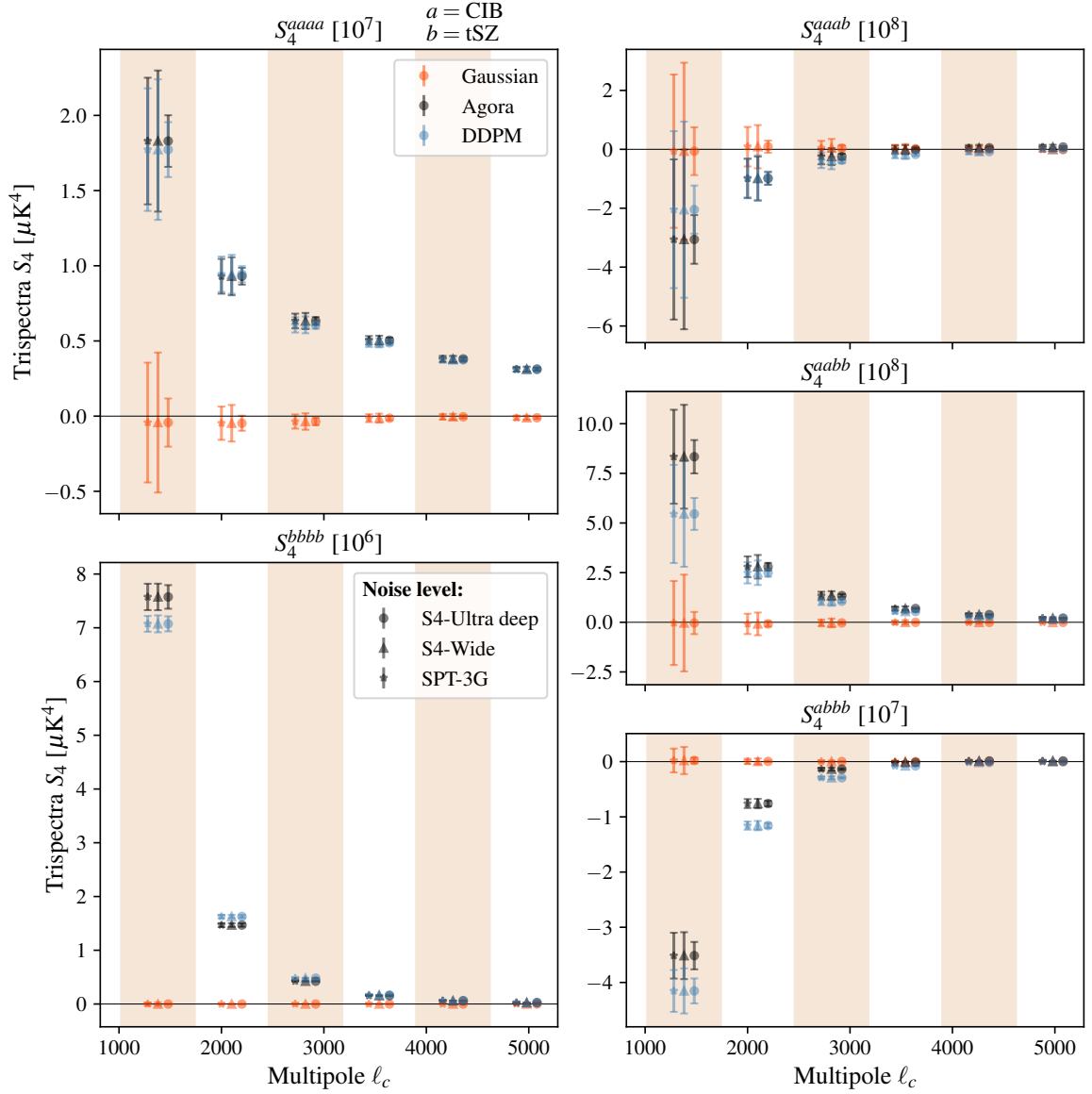


**Figure 11.** Joint trispectrum ( $S_4$ ) statistics of CIB and tSZ maps, using the same format as Figure 10.

and *Astroparticle Physics* **2020**, 012 (2020).

- [23] Y. Omori, *Monthly Notices of the Royal Astronomical Society* **530**, 5030 (2024), <https://academic.oup.com/mnras/article-pdf/530/4/5030/57527656/stae1031.pdf> .
- [24] D. Han, N. Sehgal, and F. Villaescusa-Navarro, *Phys. Rev. D* **104**, 123521 (2021), [arXiv:2105.11444 \[astro-ph.CO\]](https://arxiv.org/abs/2105.11444) .
- [25] M. Mebratu and W. L. K. Wu, *arXiv e-prints* , [arXiv:2505.21220](https://arxiv.org/abs/2505.21220) (2025), [arXiv:2505.21220 \[astro-ph.CO\]](https://arxiv.org/abs/2505.21220) .
- [26] T. Flöss, W. R. Coulton, A. J. Duivenvoorden, F. Villaescusa-Navarro, and B. D. Wandelt, *MNRAS* **533**, 423 (2024), <https://academic.oup.com/mnras/article-pdf/533/1/423/58786991/stae1818.pdf> .

- [27] S. D. Aoyama, K. Osato, and M. Shirasaki, [arXiv e-prints](#), [arXiv:2505.00345 \(2025\)](#), [arXiv:2505.00345 \[astro-ph.CO\]](#).
- [28] N. Mudur and D. P. Finkbeiner, [arXiv e-prints](#), [arXiv:2211.12444 \(2022\)](#), [arXiv:2211.12444 \[astro-ph.CO\]](#).
- [29] J. Sohl-Dickstein, E. Weiss, N. Maheswaranathan, and S. Ganguli, in *Proceedings of the 32nd International Conference on Machine Learning*, Proceedings of Machine Learning Research, Vol. 37, edited by F. Bach and D. Blei (PMLR, Lille, France, 2015) pp. 2256–2265.
- [30] J. Ho, A. Jain, and P. Abbeel, in *Advances in neural information processing systems*, Vol. 33 (2020) p. 6840–6851.
- [31] Y. Song, J. Sohl-Dickstein, D. P. Kingma, A. Kumar, S. Ermon, and B. Poole, [CoRR abs/2011.13456 \(2020\)](#), [2011.13456](#).
- [32] A. Klypin, G. Yepes, S. Gottlöber, F. Prada, and S. Heß, [Monthly Notices of the Royal Astronomical Society](#) **457**, 4340 (2016), <https://academic.oup.com/mnras/article-pdf/457/4/4340/18515365/stw248.pdf>.
- [33] A. van Engelen, S. Bhattacharya, N. Sehgal, G. P. Holder, O. Zahn, and D. Nagai, [ApJ](#) **786**, 13 (2014), [arXiv:1310.7023 \[astro-ph.CO\]](#).
- [34] M. S. Madhavacheril and J. C. Hill, [Physical Review D](#) **98**, 023534 (2018), [arXiv:1802.08230 \[astro-ph.CO\]](#).
- [35] N. Sailer, E. Schaan, and S. Ferraro, [Physical Review D](#) **102**, 063517 (2020), [arXiv:2007.04325 \[astro-ph.CO\]](#).
- [36] N. MacCrann, B. D. Sherwin, F. J. Qu, T. Namikawa, M. S. Madhavacheril, *et al.*, [arXiv e-prints](#), [arXiv:2304.05196 \(2023\)](#), [arXiv:2304.05196 \[astro-ph.CO\]](#).
- [37] M. Doohan, M. Millea, S. Raghunathan, F. Ge, L. Knox, K. Prabhu, C. L. Reichardt, and W. L. K. Wu, [JCAP](#) (2025), [arXiv:2502.20801 \[astro-ph.CO\]](#).
- [38] G. Fabbian, A. Lewis, and D. Beck, [JCAP](#) **2019**, 057 (2019), [arXiv:1906.08760 \[astro-ph.CO\]](#).
- [39] Y. Omori, E. J. Baxter, C. Chang, *et al.*, [Physical Review D](#) **107**, 023529 (2023), [arXiv:2203.12439 \[astro-ph.CO\]](#).
- [40] J. A. Sobrin, A. J. Anderson, A. N. Bender, *et al.*, [ApJS](#) **258**, 42 (2022), [arXiv:2106.11202 \[astro-ph.IM\]](#).
- [41] I. G. McCarthy, J. Schaye, S. Bird, and A. M. C. Le Brun, [MNRAS](#) **465**, 2936 (2017), [arXiv:1603.02702 \[astro-ph.CO\]](#).
- [42] A. J. Mead, T. Tröster, C. Heymans, L. Van Waerbeke, and I. G. McCarthy, [A&A](#) **641**, A130 (2020), [arXiv:2005.00009 \[astro-ph.CO\]](#).
- [43] P. Behroozi, R. H. Wechsler, A. P. Hearin, and C. Conroy, [Monthly Notices of the Royal Astronomical Society](#) **488**, 3143–3194 (2019).
- [44] K. M. Górski, E. Hivon, A. J. Banday, B. D. Wandelt, F. K. Hansen, M. Reinecke, and M. Bartelmann, [ApJ](#) **622**, 759 (2005), [arXiv:astro-ph/0409513 \[astro-ph\]](#).
- [45] K. Abazajian, G. E. Addison, P. Adshead, *et al.*, [ApJ](#) **926**, 54 (2022), [arXiv:2008.12619 \[astro-ph.CO\]](#).
- [46] S. Raghunathan, [ApJ](#) **928**, 16 (2022), [arXiv:2112.07656 \[astro-ph.CO\]](#).
- [47] P. Wang, “denoising-diffusion-pytorch,” <https://github.com/lucidrains/denoising-diffusion-pytorch> (2022).
- [48] O. Ronneberger, P. Fischer, and T. Brox, in *Medical image computing and computer-assisted intervention – MICCAI 2015* (Springer International Publishing, Cham, 2015) p. 234–241.

- [49] A. Vaswani, N. Shazeer, N. Parmar, J. Uszkoreit, L. Jones, A. N. Gomez, L. u. Kaiser, and I. Polosukhin, in *Advances in Neural Information Processing Systems*, Vol. 30 (2017).
- [50] S. Stamatelopoulos and T. P. Sapsis, *Computer Methods in Applied Mechanics and Engineering* **435**, 117589 (2025).
- [51] J. Schmalzing, M. Kerscher, and T. Buchert, in *Dark Matter in the Universe*, edited by S. Bonometto, J. R. Primack, and A. Provenzale (1996) p. 281, [arXiv:astro-ph/9508154 \[astro-ph\]](#) .
- [52] A. M. P. Boelens and H. A. Tchelepi, *SoftwareX* **16**, 100823 (2021).
- [53] J. J. Lee, J. R. Bond, P. Motloch, A. van Engelen, and G. Stein, *Monthly Notices of the Royal Astronomical Society* **529**, 2543 (2024), <https://academic.oup.com/mnras/article-pdf/529/3/2543/57035729/stae605.pdf> .
- [54] J. C. Hill, E. J. Baxter, A. Lidz, J. P. Greco, and B. Jain, *Physical Review D* **97**, 083501 (2018), [arXiv:1706.03753 \[astro-ph.CO\]](#) .
- [55] J. R. Bond, B. J. Carr, and C. J. Hogan, *ApJ* **367**, 420 (1991).
- [56] M. Millea and U. Seljak, [arXiv:2112.09354 \[astro-ph, stat\]](#) (2021), [arxiv:2112.09354 \[astro-ph, stat\]](#) .
- [57] Z. Wang, Y. Jiang, H. Zheng, P. Wang, P. He, Z. Wang, W. Chen, and M. Zhou, [arXiv e-prints](#) , [arXiv:2304.12526 \(2023\)](#), [arXiv:2304.12526 \[cs.CV\]](#) .
- [58] P. Dhariwal and A. Nichol, [arXiv e-prints](#) , [arXiv:2105.05233 \(2021\)](#), [arXiv:2105.05233 \[cs.LG\]](#) .
- [59] A. Grover, M. Dhar, and S. Ermon, [arXiv e-prints](#) , [arXiv:1705.08868 \(2017\)](#), [arXiv:1705.08868 \[cs.LG\]](#) .
- [60] B. Thorne, J. Dunkley, D. Alonso, and S. Naess, *MNRAS* **469**, 2821 (2017), [arXiv:1608.02841 \[astro-ph.CO\]](#) .
- [61] Q. Zhang and Y. Chen, [arXiv e-prints](#) , [arXiv:2110.07579 \(2021\)](#), [arXiv:2110.07579 \[cs.LG\]](#) .
- [62] T. Salimans and J. Ho, in *International Conference on Learning Representations* (2022).
- [63] D. P. Kingma, [arXiv preprint arXiv:1412.6980](#) (2014).